1 **Physical mechanisms for biological carbon uptake during the onset of the spring**

2 **phytoplankton bloom in the northwestern Mediterranean Sea (BOUSSOLE site)**

3 Liliane Merlivat[1], Michael Hemming [2], Jacqueline Boutin[1], David Antoine[3, 4], Vincenzo

4 Vellucci[5], Melek Golbol[5], Gareth A. Lee[6], Laurence Beaumont[7]

5 [1] Sorbonne Université, CNRS/IRD/MNHN, LOCEAN, IPSL, Paris, France

6 [2] Coastal and Regional Oceanography Lab, School of Mathematics and Statistics, University

7 of New South Wales, Sydney, New South Wales, Australia

8 [3] Remote Sensing and Satellite Research Group, School of Earth and Planetary Sciences,

9 Curtin University, Perth, WA 6845, Australia

10 [4] Sorbonne Université, CNRS, Laboratoire d'Océanographie de Villefranche, Villefranche sur

11 Mer 06230, France

12 [5] Sorbonne Université, CNRS, Institut de la Mer de Villefranche, Villefranche sur Mer 06230,

13 France

14 [6] Centre for Ocean and Atmospheric Sciences, School of Environmental Sciences, University

15 of East Anglia, Norwich Research Park, Norwich NR4 7TJ, UK

16 [7] Division Technique INSU-CNRS, 92195 Meudon CEDEX, France

18 Correspondence to: liliane.merlivat@gmail.com

19 Keywords : Bloom onset ; Carbon uptake ; Air-sea interaction; Mediterranean sea

20 Abstract

21 Several trigger mechanisms have been proposed for the onset of the phytoplankton spring

22 bloom. Among these, that phytoplankton cells begin to bloom when they experience higher

23 average light levels in shallower mixed layers, a result of the surface net heat fluxes becoming

24 positive and wind strength decreasing. We study the impact of these two forcings in the

25 northwestern Mediterranean Sea. We take advantage of hourly measurements of oceanic and

26 atmospheric parameters collected at two neighboring moorings during the months of March

27 and April in the years 2016 to 2019, combined with glider data in 2016. The onset of the

28 surface phytoplankton growth is concomitant with the start of significant biological activity

29 detected by a sudden decrease in dissolved inorganic concentrations derived from

30 measurements in the upper 10 m of the water column. A rapid reduction in wind stress

31 following high-wind events is observed at the same time. A resulting shallow mixing layer

32 favors carbon uptake by phytoplankton lasting a few days. Simultaneously, the air-sea net

33 heat flux switches from negative to positive linked to changes of the latent air-sea heat flux,

34 which is proportional to the wind speed. This results in an increased thermal stratification of

35 the ocean's surface layers. In 2016, glider data show that the mixing layer is significantly

36 shallower than the mixed layer at the onset of the surface phytoplankton bloom. We conclude

37 that decreases in the mixing and mixed layer depths lead to the onset of the phytoplankton

38 bloom due to the relaxation of wind speed following storms. We estimate net daily

39 community production in the mixing layer over periods of 3 days between 2016 and 2019 as

40 between 38 mmol C m^{-2} and 191 mmol C m^{-2}. These results have important implications as

41 biological processes play a major role in the seasonal evolution of surface pCO2 and thereby

42 the rate of reduction of atmospheric CO_2 by exchange at the air-sea interface.

43

44

45

46 Introduction

47 Investigating the physical and biological mechanisms contributing to changes in air-sea

48 carbon dioxide (CO_2) fluxes is essential as it is a critical component of the global carbon

49 cycle and the climate system with the ocean removing about a quarter of the CO_2 emitted into

50 the atmosphere by human activities over the last decade. It depends on the gradient of CO_2

51 partial pressure, pCO_2, between the atmosphere and the surface ocean [Takahashi et al., 2009;

52 Rödenbeck et al., 2013; Merlivat et al., 2015]. pCO_2 in the ocean mixed surface layer depends

53 on the relative contribution of dynamic transport, thermodynamics and biogeochemistry. As

54 the biological carbon pump lowers pCO_2 and Dissolved Inorganic Carbon (DIC) at the sea

55 surface, the production of plankton biomass during a bloom can be sufficient to reverse the

56 annual cycle of surface-ocean CO_2 uptake. A decrease in surface DIC, after the impact of

57 physical processes have been eliminated, essentially indicates the beginning of the

58 phytoplankton spring growth. Conceptual frameworks have been proposed to explain when

59 the depth integrated phytoplankton biomass starts accumulating during blooms [Behrenfeld,

60 2010; Sverdrup, 1953]. The timing of the initiation of the surface spring phytoplankton bloom

61 depends in particular on atmospheric forcing. The physical processes of wind stress, heat flux

62 and vertical mixing control the depth of the mixed/mixing layer and thus the availability of

63 light [Siegel et al, 2002, Chiswell, 2011; Taylor and Ferrari, 2011; Brody and Lozier, 2015;

64 Enriquez and Taylor, 2015, Rumyantseva et al, 2019].   Thus, to better understand which

65 fundamental physical processes control the timing of the onset of the surface bloom, in situ

66 measurements are needed at the appropriate hourly to daily timescale. It is important to draw

67 attention to the atmospheric forcing timescale. In biogeochemical ocean modeling studies,

68 typically built on atmospheric models, reanalysis or satellite data, time resolution of at best a

69 few days are required [Mahadevan et al, 2012]. Attendre reponse Michael
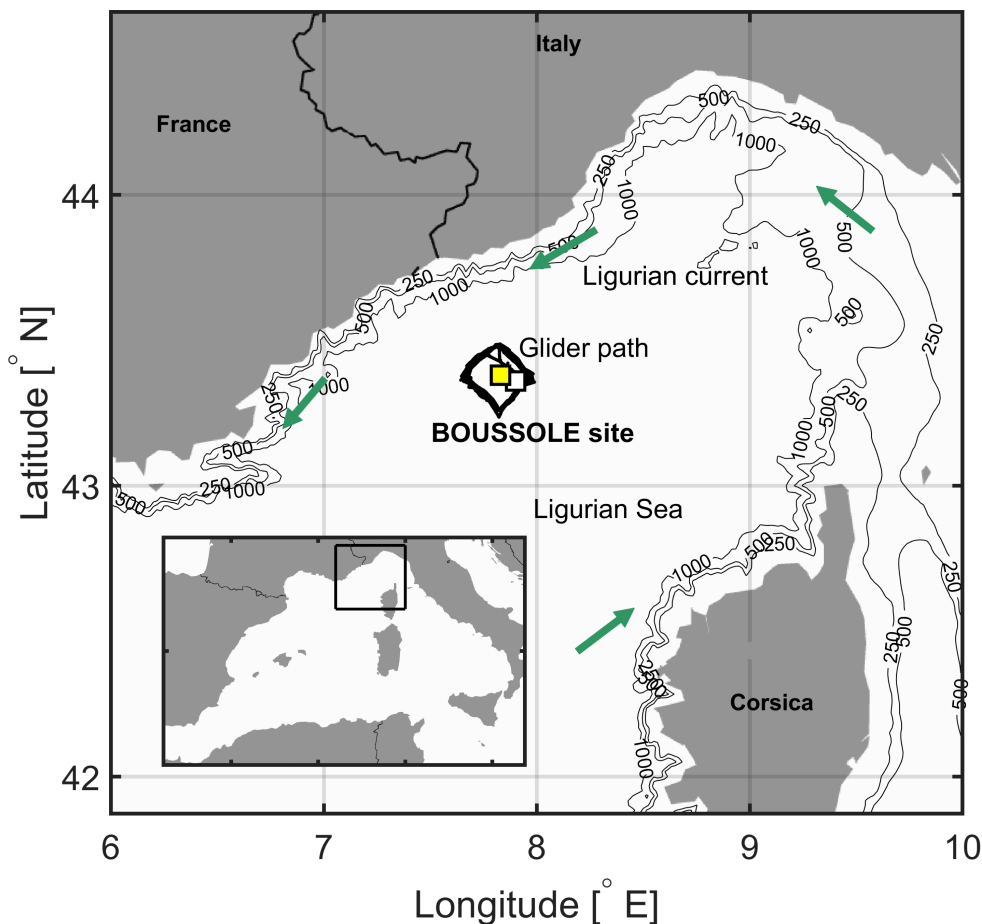
70

71 Figure 1. The area of the northwestern Mediterranean Sea showing the French and Italian

72 Rivieras, the island of Corsica, the main current branches (green arrows) in the Ligurian Sea

73 and the location of the BOUSSOLE buoy (white square) and the AZUR meteorological buoy

74 (yellow square). The black line indicates the glider's path in March-April 2016.

In the northwestern Mediterranean Sea, the BOUSSOLE buoy (Bouée pour l'acquisition de Séries Optiques à Long Terme; Antoine et al., 2006, 2008a,b) is located in the central area of the Liguro-Provençal basin (Fig.1), where the dominant ocean currents are generally weak (<20 cm s^{-1}) [Millot, 1999; Antoine et al., 2008b; Niewiadomska et al., 2008]. The main processes that govern the pCO$_2$ variations at the sea surface on an annual scale, after removal of the temperature effect, are vertical convective mixing and biological production [Begovic and Copin-Montégut, 2002; Copin-Montégut al., 2004; Hood and Merlivat, 2001; Merlivat et al., 2018 Intense convection resulting from repeated high wind events in winter or early spring when atmospheric temperatures are typically low brings nutrients to the surface layer [Andersen and Prieur, 2000; Antoine et al., 2008b; Marty et al., 2002; Pasqueron de Fommervault et al., 2015].

The objective of this study is to examine the impact of atmospheric forcing on surface phytoplankton bloom initiation in the northwestern Mediterranean Sea. To this aim we use concurrent hourly data of seawater carbon chemistry measured at depths less or equal to 10 m at the BOUSSOLE mooring [Merlivat et al, 2018] and atmospheric flux measurements at the Azur meteorological buoy 3.1 nm (5.8 km) away from BOUSSOLE in March and April 2016 to 2019. Additional measurements of phytoplankton chlorophyll-a (Chla), temperature and density were provided by an underwater glider deployed in March-April 2016. The initiation of biological carbon uptake is revealed by the sudden decrease in DIC measured at the BOUSSOLE buoy.

In the Material and Methods section, we provide the description of data processing, theoretical framework, and calculations used to evaluate mixing regimes in the water column and net community production. The results section presents measured atmospheric and biogeochemical parameters observed in March-April, and NCP estimates from 2016 to 2019. The Discussion section relates our results to previous findings and presents our conclusions regarding the drivers of phytoplankton bloom initiation.

2 Material and methods

2.1- Data from the BOUSSOLE mooring

CARIOCA sensors [Merlivat and Brault, 1995] installed on the BOUSSOLE buoy (43°22'N, 7°54'E; Fig.1) monitored hourly partial pressure, pCO$_2$, at both 3 and 10 m alongside salinity

106 and temperature (SEABIRD Scientific SBE 37 MicroCAT CTDs). Protocols for calibration of
107 in situ measurements are described in [Merlivat et al, 2018]. CARIOCA measurements of
108 pCO_2 and temperature are combined with total alkalinity (Alk) derived from salinity
109 [Merlivat et al., 2018] to calculate DIC. The dissociation constants of Mehrbach et al., (1973)
110 refitted by Dickson and Millero (1987) are used, as recommended by Alvarez et al. (2014) for
111 the Mediterranean Sea. For the March-April months mean salinity is 38.3, corresponding with
112 mean Alk equal to 2571.4 µmol kg^{-1} [Copin et al, 2004]. The expected precision of the
113 CARIOCA pCO_2, and DIC is 5 µatm, and 3 µmol $kg^{-1,}$ respectively [Merlivat et al, 2018].

114 2.2- Glider observations

115 An iRobot Seaglider model 1KA (SG537) with an ogive fairing operated by the University of
116 East Anglia (UEA) [see Hemming et al., 2017] was deployed during the BOUSSOLE
117 monthly cruise (#169) [Golbol et al 2000] and recovered 1 month later with a ship of
118 opportunity. Diving to 1000 m, 147 dives were completed between March 7 and April 5 2016
119 repeatedly-sampling a square-shaped path surrounding the BOUSSOLE buoy (Fig. 1) with
120 corners pointing to cardinal directions. Out of 147 dives, a number of them contain data that
121 are within 10 km of the BOUSSOLE mooring, i.e. when it was sampling in the eastern corner
122 of the diamond path. The glider was equipped with a non-pumped SEABIRD Scientific SBE
123 9 CTD instrument package providing temperature and salinity, and a WET Labs Eco Puck
124 sensor providing relative phytoplankton Chla fluorescence, factory calibrated into Chla
125 concentration units (mg m^{-3}).

126 2.3- Azur meteorological buoy

127 The Azur meteorological buoy has been deployed since 1999 by the French weather forecast
128 Agency (Meteo-France) at 43°23'N, 7°50'E (Fig. 1). It provides hourly measurements of
129 surface wind speed extrapolated to 10 m height, U_{10} (m s^{-1}), net long wave radiation, net short-
130 wave radiation, and the sensible and latent heat fluxes. These are needed to estimate the net
131 air-sea heat budget at the sea surface (http://mistrals.sedoo.fr). U_{10} is used to calculate wind
132 stress, τ, as follows: $\tau = \rho_a\, C_d\, U_{10}^2$, where ρ_a is air density (1.2 kg m^{-3}), and C_d is the drag
133 coefficient (1.4 x 10^{-3}). Photosynthetically Active Radiation (PAR, mol photons m^{-2} d^{-1}) is
134 related to solar irradiance (i.e. short-wave flux), SW, following PAR = 0.473 SW
135 [Papaioannou et al., 1993].

136 2.4- Estimation of mixed and mixing layer depths

137   The mixing layer depth, Z_{mx}, is the upper part of a mixed layer of uniform density where

138   active turbulence occurs [Brainerd and Gregg 1995]. Several recent studies have highlighted

139   the significance of this layer to understand the phytoplankton phenology of phytoplankton

140   blooms [Brody and Lozier, 2015; Taylor and Ferrari, 2011]. Autonomous profiling floats

141   equipped with bio-optical sensors have also highlighted the importance of mixing rather than

142   mixed layers to characterize the onset and the development of a phytoplankton bloom. Wind-

143   driven and buoyancy-driven regimes control the characteristics and depth of active mixing

144   [Brody and Lozier, 2014, 2015, Ramuyantseva et al, 2015, Lacour et al, 2019, Pellichero et al,

145   2020]. Wind-driven mixing dominates in the presence of weak buoyancy forcing when heat

146   fluxes are small. In that case, the dominant mixing length scale is equal to the Ekman length

147   layer depth scale.

148   The daily mean mixed layer depth, Z_{ml} is derived for 2016 from glider vertical profiles of

149   temperature and salinity using the algorithm provided by Holte and Talley, (2009) estimated

150   using the potential density algorithm.

151   To estimate Z_{mx}, τ is used to calculate the Ekman layer depth, Z_{ek}, $Z_{ek}=\gamma\, u_*/f$, where γ is an

152   empirical constant (0.5), f is the Coriolis parameter (10^{-4} s^{-1}) over the BOUSSOLE area, and

153   u_* is the turbulent friction velocity, $u_* = \sqrt{\dfrac{\tau}{\rho_w}}$ (m s^{-1}), with ρ_w the density of the surface sea

154   water [Lacour et al, 2019]. When heat fluxes are large and positive, Enrikez and Taylor

155   (2015) proposed to express the mixing depth Z_{mx} in terms of the surface forcing, i.e. the

156   surface stress and a stabilizing surface buoyancy flux B_0, as follows:

157
$$\frac{1}{Z_{mx}^2} = \frac{f^2}{(C_3\ u_*)^2} + \frac{f\, B_0}{(C_4\ u_*^2)^2} \qquad (1)$$

158   With $C_3=1$, $C_4=0.57$, $B_0 = Q\,\lambda\, g\, /c_p\,\rho_0$, where Q is the net surface heat flux, λ the thermal

159   expansion coefficient (1.65 10^{-4} °C^{-1}), g the gravitational acceleration (9.81 m s^{-2}), c_p the

160   specific heat of water (4 10^{-3}J kg^{-1} °C^{-1}) and ρ_0 the pure water density (1000 kg m^{-3}).

161   2.5-Estimation of euphotic zone depth

162   The euphotic depth, Z_{eu}, is generally derived as the depth where PAR is 1% of its surface

163   value. Z_{eu} can be estimated from Chla at the surface using the method described by Lee et al.

164   (2007) based on the equation of Morel and Berthon (1989):

165
$$Z_{eu} = 34\ (\text{Chla})^{-0.39} \qquad (2)$$

For the period between 2017 and 2019, GlobColour merged Chla products were used, which are based on satellite observations with a resolution of 25 km, and a binning period of 8 days (http://www.oceancolour.org). For 2016, glider surface Chla was used to derive Zeu instead of satellite measurements. We excluded glider Chla between 05:00 and 20:00 UTC affected by sunlight–induced fluorescence quenching, and we applied a depth-constant offset to glider measurements using Chla water samples available on March 7.

2.6-Estimation of average mixing layer irradiance

We calculate the average mixing layer irradiance, I, function of the incident surface irradiance, PAR, mixing layer depth, h, and the diffuse attenuation coefficient, K_d, estimated from surface chlorophyll-a concentrations (Venables and Moore, 2010).

$$K_d = 0.05 + 0.057 \, Chla^{0.58}$$

$$I = \frac{PAR}{K_d h} (1 - e^{-K_d h})_- \quad (3)$$

2.7 – Estimation of net community production

Biological Net Community Production rates, NCP (mmol m^{-2} day^{-1}), are calculated for separate 3-day periods in March-April, 2016 to 2019 from DIC concentrations derived from CARIOCA measurements, assuming that measurements in the top 10 m of the water column are representative of an homogeneous mixing layer [Boutin and Merlivat, 2009; Merlivat et al, 2015; Pelicherro et al, 2020]. In the study area, current velocities are expected to be small [Millot, 1999; Antoine et al., 2008; Niewiadomska et al., 2008]. Vertical mixing events are identified by an increase in DIC resulting from upward movement of high DIC Levantine Intermediate Water (LIW) at approximately 200 m depth [Copin-Montégut and Bégovic, 2002] To estimate NCP, we ascertain that the contribution of horizontal advection was negligible. We isolated time periods when local physical processes were largely one-dimensional in order to study changes in biological and chemical parameters that occurred during rapid transitions from deep mixing to intermittent stratification. In 2016, over a four-day period, March 18-21, the diurnal cycle of DIC values characterized by a maximum in the morning followed by a minimum at the end of the day indicates the onset of organic matter formation. The eddy diffusion term is negligible as the DIC gradient at the base of the mixing layer is very weak, entrainment is not expected as changes in DIC are observed during periods

195   of stratification. For the identified periods, biological production and air-sea exchange are the

196   dominant processes responsible for daily changes in DIC.

197   NCP is thus estimated from temporal variation of the DIC integrated over Z_{mx} (DIC_{int}), and

198   corrected for the air-sea CO_2 flux contribution [Pelicherro et al, 2020]:

199     $$NCP = \left(\frac{\Delta DIC_{int}}{\Delta t}\right)_{bio} = \left(\frac{\Delta DIC_{int}}{\Delta t}\right)_{meas} - k \times s \times (pCO_{2atm} - pCO_{2sw}) \quad (4)$$

200   The first term in equation 4, $\left(\frac{\Delta DIC_{int}}{\Delta t}\right)_{meas}$, is the daily variation of DIC_{int} calculated over 3

201   days from the date identified as the start of phytoplankton bloom (t_0) , whilst the remaining

202   part corresponds to DIC variability due to air-sea CO_2 exchange, where k is the gas transfer

203   velocity [Wanninkhof, 2014], s is the solubility of CO_2 in seawater [Weiss, 1974], and

204   pCO_{2sw} and pCO_{2atm} are respectively the partial pressures of CO_2, in µatm, in sea water and in

205   air [Merlivat et al, 2018].

206   3 Results

207   3.1- Description of the 2016 time-series
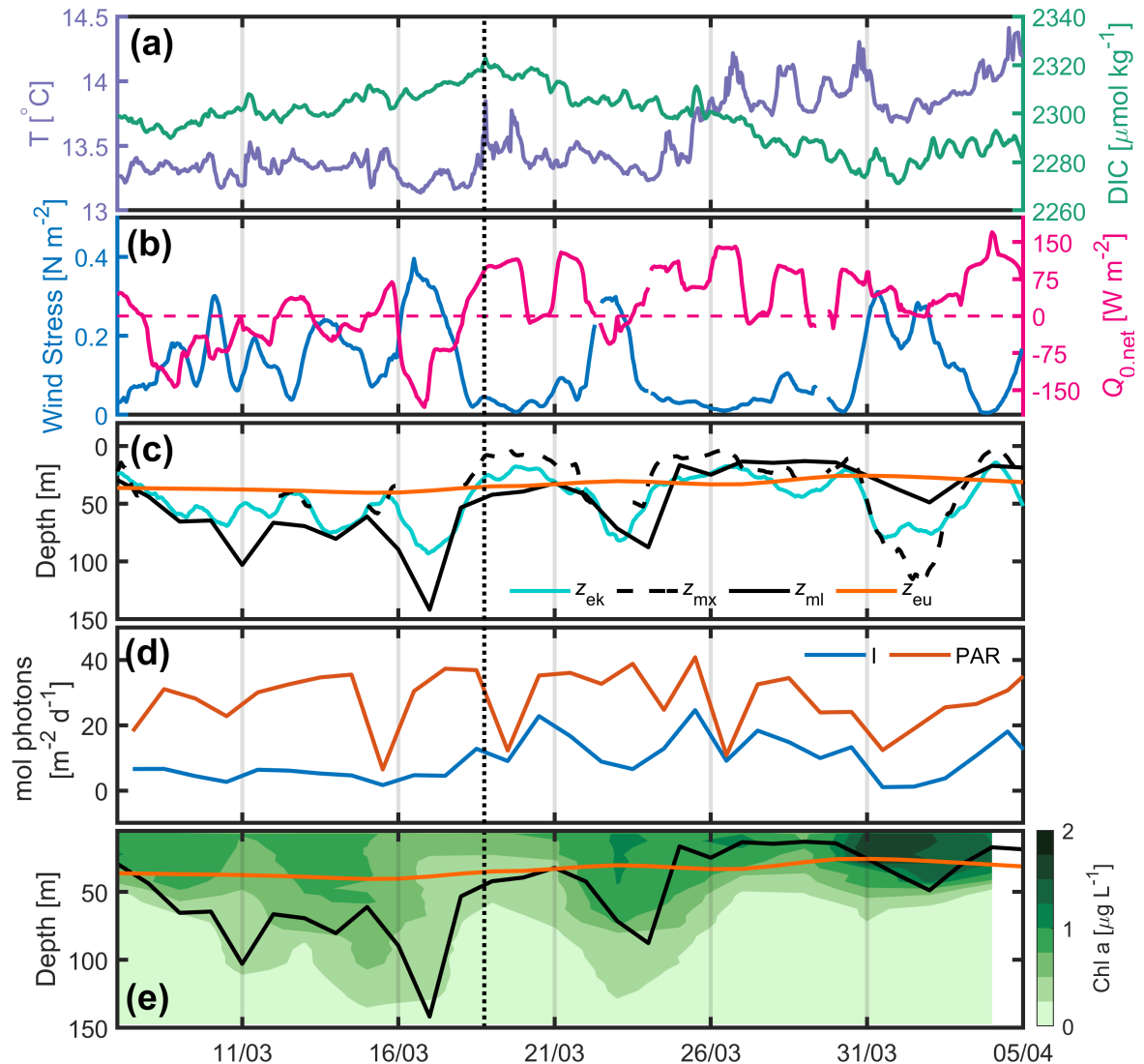
Figure 2. 2016 (a) Hourly DIC (green) and SST(purple) at the BOUSSOLE site, (b) hourly wind stress (blue) and net heat flux (pink) at the Azur buoy site. The pink dotted line indicates the change of sign of the net heat flux from negative to positive values, (c) daily depths of the mixed layer (black), mixing layer (dotted black), Ekman layer (cyan) and euphotic layer (orange) at the BOUSSOLE site. The black dotted line on panels (a), (b), (c) (d) and (e) indicates the onset time of the bloom (March 18). (d) PAR (orange) and I, average mixing layer irradiance (blue), (e) Glider-derived depths of the mixed layer (black curve, same as in (c)), euphotic layer (orange), and nighttime 2-day binned chlorophyll concentration (green coloring) retrieved between March 7 and April 5.

The temporal evolution of physical and biogeochemical parameters between March 7 and April 5 2016 is displayed in Fig. 2. It shows an initial increase in DIC until March 18 (Fig. 2a), resulting from the vertical mixing of surface waters with the DIC-enriched underlying LIW [Copin-Montégut and Bégovic, 2002], followed by a decrease in DIC that corresponds to an increase of surface Chla (Fig 2e). Temperature increases intermittently over the same time period (Fig. 2a), with a sharp increase on March 18 and 25. Before March 18 frequent atmospheric fronts associated with wind forcing between 0.2 and 0.5 N m^{-2} were observed (Fig. 2b). $Q_{0,net}$ was negative most of the time leading up to March 18, but mostly positive afterwards (Fig. 2b). A clear anticorrelation was observed between τ and $Q_{0,net}$ (Fig. 2b). The mixed-layer depth derived from the glider measurements (< 20 km away from the Boussole site) deepened to > 70 m at times between March 8 and March 18, consistent with the passage of frequent atmospheric fronts. From March 18 to April 5, Z_{ml} shoaled from ~ 45 m to ~10 m, excluding two short periods around March 24 and April 2 when atmospheric fronts were passing (Fig. 2c). From March 18 to 31, Z_{mx} was for a considerable time either shallower than, or at similar depth to Z_{ml} and Z_{eu} (Fig. 2c). The start of the increase in PAR from March 15 precedes the increase in irradiance by 3 days as a result of the decrease of the mixing layer depth observed only after March 18 (Fig. 2d**).**

From March 18 to April 5, an increase in glider Chla was observed in the upper layer (Fig. 2e) as the result of the biomass accumulation within the water column following the initial growth of surface phytoplankton [Behrenfeld, M. and E. Boss, 2014]. The same was observed in the Southern Ocean [Pelicherro et al, 2019].

3.2- Description of the 2017-2018-2019 time-series

Only measurements at the BOUSSOLE and Azur buoys were available between 2017 and 2019. Here we focus on the periods between March 1 and April 25. In 2017, from March 9, after the passage of a very active atmospheric front (τ up to 2.7 N m^{-2}), a decrease in DIC accompanied by an increase in temperature was observed for a period of 14 days despite a few short bursts of vertical mixing, typically lasting less than 1 day (Fig.3a, d, g). At the same time, the net surface heat flux switched from negative to positive most of the time. Over this 14-day period, Z_{mx} was predominantly shallower than the Z_{eu} at times when DIC was decreasing.

In 2018 (Fig. 3b, e, h) and 2019 (Fig. 3c, f, i), the weather records throughout the month of March are very similar, showing a succession of very strong wind events at the start of the

249 investigated time periods, with τ values of up to 3.7 N m^{-2} and Z_{ek} values as deep as 300 m.

250 On April 5, 2018, following a period of high wind stress resulting in the formation of a deep

251 mixing layer (~250 m), a decrease in DIC and an increase in SST were observed over 3 days.

252 At the same time, the net heat flux oscillated around zero. In 2019, CARIOCA data were only

253 available after March 24. On March 30, 3 days after high winds, a decrease in DIC and an

254 increase in temperature lasted 3 days, while simultaneously the net heat flux reversed from

255 negative to positive.

256
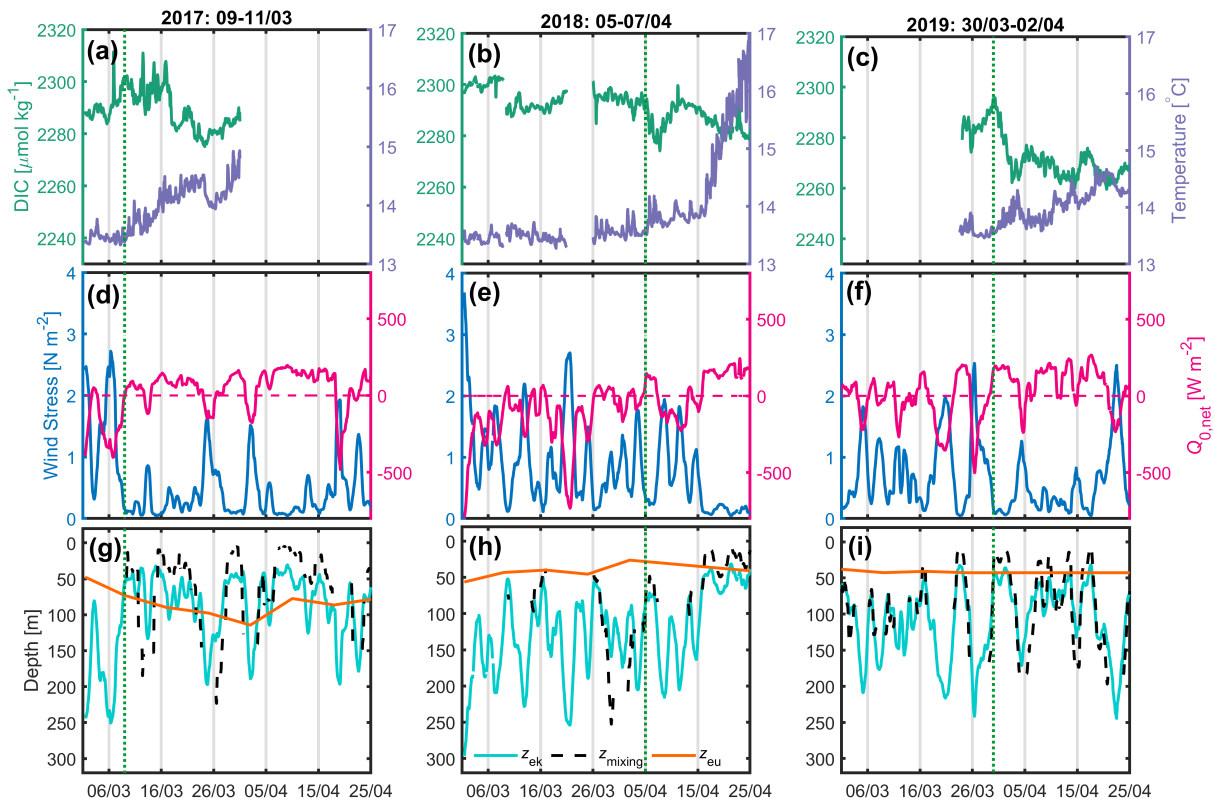
257

258 Figure 3. (a, b, c) 2017, 2018 and 2019 DIC (green) and SST (purple) at the BOUSSOLE site,

259 (d, e, f) wind stress (blue) and net heat flux (red) at the Azur buoy site. (d, e, f) The red dotted

260 line indicates the change of sign of the net heat flux from negative to positive values, (g, h, i)

261 depths of the mixing layer (dotted black), Ekman layer (cyan) and euphotic layer (orange) at

262 the BOUSSOLE site. The vertical dotted green line indicates the onset of the decrease of DIC.

263 For the period between 2017 and 2019, only satellite chlorophyll-a concentrations with a

264 binning period of 8 days were available, which is too large to calculate the average mixing

265 irradiance as it is highly variable on a daily scale (Fig 2.d).

266 3.3- NCP

267 NCP was estimated (Eq. 3) for 3-day periods over the four time-series between 2016 and
268 2019 (Table 1). Because we compute NCP only during periods when Z_{ml} and Z_{mx} shoal and
269 the air-sea CO_2 flux is very small, the measured total daily changes of DIC, dDIC/dt
270 (correlation coefficient, r^{*2} >0.70), is expected to represent the biological consumption of
271 DIC. In 2016, 2017, and 2019, daily biological carbon uptake fluxes are between 38 and 191
272 mmol $m^{-2} d^{-1}$. PAR and I vary respectively from 30 to 53 and 13 to 25 mol photons $m^{-2} d^{-1}$
273 for the four considered periods (Table 2).

	T_0	dDIC/dt [a]	r^{*2} [b]	$\Delta DIC / \Delta t$ [c]	r^{*2} [d]	air-sea flux CO_2 [e]	NCP [f]
		µmol $kg^{-1}d^{-1}$		mmol $m^{-2}d^{-1}$		mmol $m^{-2}d^{-1}$	mmol $m^{-2} d^{-1}$
2016 10m	March 18	-3.0	0.80	-37	0.68	1	38
2017 3m	March 9	-4.5	0.84	-188	0.86	3	191
2018 3m	April 5	-6.5	0.70			17	
2019 10m	March 30	-8.3	0.93	-163	0.63	4	167

274

275 Table 1. Net community production computed in the mixing layer over 3 days (NCP) after the
276 bloom onset (T_0). (a, b) variation of DIC at the measurement depth and linked correlation
277 coefficient; (c, d) change of integrated DIC over Z_{mx} and linked correlation coefficient ;(e)
278 CO_2 flux from the atmosphere to the ocean; (f), absolute value of calculated NCP is
279 considered in order to provide positive values throughout the presentation and discussion in
280 the manuscript.

281

282 4 Discussion

283 4.1 Analysis of the physical drivers of the bloom initiation over the 4 years, 2016-2019

284 4.1.1 In 2016, the consumption of carbon indicated by the decrease in DIC from March 18
285 attests the initiation of the formation of phytoplankton biomass (Fig. 2,). Between 2

286   successive days, March 17 and 18, a rapid decrease in daily wind stress from 0.24 to 0.04 N

287   m^{-2} results in a change of sign of the net heat flux from -68 to +56 W m^{-2} (Fig.4a) and a

288   shoaling Z_{mx}, which is for the most part shallower than Z_{eu} (Fig.4b) after March 18.

289
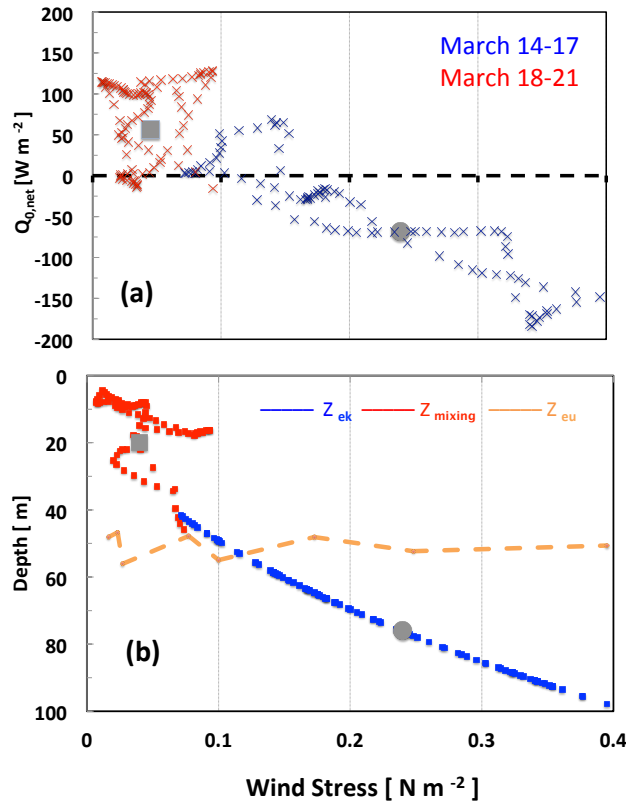
290   Figure 4. Changes of physical parameters (hourly values) at the onset of the 2016 bloom

291   during 2 consecutive periods of 4 days, March 14-17 (blue) and March 18-21 (red) as a

292   function of wind stress (a) net surface heat flux (b) depths of the mixing layer. Grey circles

293   and grey squares indicate mean values respectively on March 17 and March 18. For

294   comparison, the orange line shows the euphotic layer depth (March 14-21).

295   This illustrates the very fast change in heat flux and mixing layer thickness resulting from the

296   decrease in wind stress. The main drivers to explain the initiation of near surface spring

297   phytoplankton blooms proposed by [Taylor and Ferrari, 2011, Brody-Lozier, 2014, 2015] are

298   a decrease in wind strength, a positive surface heat flux, and a decrease in the dominant

299   mixing length scale. Our results indicate that a decrease in τ is a common component for these

300   last two mechanisms (Fig.4). The variability of $Q_{0,net}$ is strongly controlled by the variability

301   of the latent heat flux proportional to the wind speed. From March 17 to 18, the latent heat

302 flux changed by 84 W m^{-2} representing nearly 2 thirds of the total change of Q_0, with the
303 remainder originating from an increased short-wave flux. Hence, $Q_{0,net}$ increased as τ
304 decreased. In the same way Z_{mx}, which is related to τ and $Q_{0,net}$, decreased. This highlights the
305 major contribution of wind stress relaxation in controlling the net surface heat flux, and
306 subsequent stratification leading to sallower Z_{mx}

307 4.1.2 Over the 4 years, 2016-2019, during the months of March and April, at the very
308 beginning of spring, the conditions required for initiating the spring bloom are very similar
309 although the range of wind stress values is smaller in 2016. (Fig. 2, Fig. 3). The wind stress
310 values are low following storm events. For all years except 2018, Z_{mx} is smaller than Z_{eu}. The
311 average atmospheric and oceanographic conditions during the onset of the bloom are shown
312 in Table 2. The decrease of wind-driven mixing is then a dominant physical mechanism,
313 namely mixed layer shoaling which best predicts the timing of the spring bloom [Brody
314 Lozier, 2014, 2015]. Likewise, in the Southern Ocean, Pelicherro et al (2020) showed that a
315 bloom is initiated only when the wind-driven mixed layer decreases, even if the net heat flux
316 has been positive for some months.

317 4.2 DIC, Chla, Irradiance at the ocean surface in 2016

318 From 18 March, over a four-day period, the diurnal cycle of DIC values (Figure 5a)
319 characterized by a maximum in the morning followed by a minimum at the end of the day
320 indicates the onset of organic matter formation. The decrease in DIC is accompanied by an
321 increase of the concentration of the glider surface Chla on March 18, and a simultaneous
322 increase in the average mixing layer irradiance is observed (Fig. 5 b). It is worth to underline
323 that the Chla maximum does not occur until 31 March, 13 days after the decrease in DIC.
324 This maximum is the one identified in most cases by the Chla satellite measurements with a
325 binning period of 8 days. As a result, this implies that these figures do not allow to accurately
326 characterise the conditions that prevail for the triggering of a bloom which are dictated by the
327 very high time variability of atmospheric forcings. Thus, due to the seasonal increase of
328 surface irradiance in March-April, as well as the availability of nutrients following vertical
329 mixing with intermediate nutrient-enriched waters [Begovic and Copin-Montégut, 2002], the
330 conditions for the onset of a bloom are met.

331

332
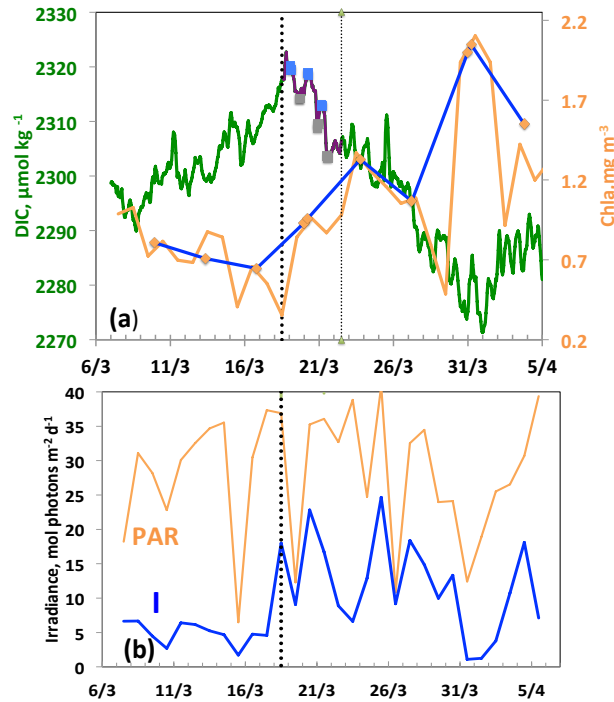
333

Figure 5. From March 6 to April 5, (a) DIC and Chla. The purple line and the squares (blue and grey) indicate the 3 days biological diurnal DIC changes during the period considered to compute NCPP. The blue and orange lines indicate the surface Chla when the glider was at a distance of less than 5 km (blue) and less than 20 km (orange) respectively from the Boussole buoy. (b) PAR and I average mixing layer irradiance. The vertical dotted black line indicates the onset of the bloom on March 18.

4.3- Biological carbon uptake

In 2016, 2017, and 2019, at the onset of the bloom Z_{mx} is shallower than Z_{eu} (Table 2). Two factors account for the observed large range of NCP variability at the time of triggering the bloom: dDIC/dt and Z_{ml}. In 2016 and 2017, DIC decreased over a period of 14 days, whereas it lasted for 3 days in 2018 and 2019, as a result of short-lived high wind events ($\tau > 1$ N m^{-2}). On April 2, 2018, a high surface phytoplankton Chla, 1.9 mg m^{-3}, was measured by satellite (Globcolour data) suggesting a strong biological signal. However, as Z_{eu} is significantly shallower than Z_{mx} (26 m vs. 65m; Fig. 3h), it would be incorrect to estimate NCP integrated over Z_{mx} using the DIC gradient measured at 3 m depth and likewise to compute the average mixing layer irradiance.

At the nearby DyFAMed site (Dynamique des Flux Atmospheriques en Mediterranee), using a 20-year O_2 time series, Coppola et al. (2018) estimated an annual net community carbon

352 production equal to 7.1 mol m^{-2} yr^{-1}, or 19.4 mmol m^{-2} d^{-1}. Additionally, using
353 determinations of primary production from ^{14}C in-situ incubations and of carbon export fluxes
354 from sediment traps at DyFAMed, Marty and Chiaverini (2002) calculated average daily
355 primary productions between 19.6 and 53 mmol m^{-2} d^{-1}. These estimates may have
356 underestimated the annual NCP values as they were calculated from monthly observations
357 while phytoplankton production varies on a daily timescale. Our DIC measurements highlight
358 the large short-term variability of carbon consumption over a few days in March-April when
359 bloom-triggering atmospheric conditions are met, such as seasonal light increase and
360 availability of nutrients.

	T_0	Wind stress $N\,m^{-2}$	Net heat flux $W\,m^{-2}$	PAR mol photons $m^{-2}d^{-1}$	Z_{mixing} m	$Z_{Euphotic}$ m	Irradiance mol photons $m^{-2}d^{-1}$
2016	March 18	0.04 +/0.02	56+/-36	37+/-3	20+/-9	47	18
2017	March 9	0.12+/-0.02	45+/-21	30+/-3	28+/-12	71	13
2018	April 5	0.30+/-0.24	127+/-12	42+/-6	62+/-9	29	
2019	March 30	0.10+/-0.02	183+/-9	53+/-2	20+/-5	43	25

361

362 Table 2.   2016-2019.   Atmospheric drivers of the onset of the bloom: average values and
363 standard deviation on the day of the start of the bloom, T_0.

364

365 5- Concluding remarks

366 Around March and April in the northwestern Mediterranean Sea, the seasonal change in
367 lighting conditions and atmospheric forcing are the essential parameters that control the
368 triggering of near-surface phytoplankton blooms. These mechanisms have been highlighted
369 through the coupling of high-frequency physical and biogeochemical in situ observations. For
370 years 2016 to 2019, a bloom started in March or early April, following a period of intense
371 mixing. The rapid decrease in surface wind speed entailed a switch from negative to positive
372 air-sea net heat fluxes, essentially due to changes in the latent air-sea heat flux proportional to
373 wind speed. These analysis support the hypothesis that decreases in the depth of active mixing,

374 a result of the transition from buoyancy-driven to wind-driven mixing, control the timing of
375 the surface spring bloom.

376 We have shown that the onset of the growth of the surface phytoplankton, identified by a
377 simultaneous initial decrease in DIC and an increase in surface Chla, precedes by a few days
378 the surface and depth integrated chlorophyll maximum detected by satellites with a binning
379 period of 8 days. This time span does not allow to identify precisely the contribution of
380 atmospheric drivers to trigger the onset of the growth of phytoplankton as it occurs on a daily
381 basis.

384 Data availability

385 BOUSSOLE data (2016-2019) are available in the SEANOE data base (Merlivat Liliane,
386 Boutin Jacqueline (2020). Mediterranean Sea surface CO_2 partial pressure and temperature
387 data. SEANOE. https://doi.org/10.17882/56709

388 Azur Meteorological buoy: http://mistrals.sedoo.fr

389 SChl, 8-day, 4 kmx4 km resolution, level 3 mapped ocean color product distributed by the
390 European Space Agency, available at http://www.ocean colour/org

391 All glider data will be archived at the British Oceanographic Data Centre
392 (BODC, https://www.bodc.ac.uk/data/bodc_database/gliders/) prior to article acceptance.

393 Author contributions: VV and MG were respectively in charge of the BOUSSOLE mooring
394 buoy maintenance and monthly water sampling. LB was responsible for the laboratory
395 preparation and calibration of the CARIOCA sensors. GAL led the UEA glider mission in
396 March-April 2016. DA and VV provided data and funding through the BOUSSOLE project
397 and contributed to writing and editing of the manuscript.

398 The authors declare that they have no conflict of interest.

399 Acknowledgments: Michael Hemming was a PhD student at the University of East Anglia
400 and Sorbonne University under the supervision of Prof. Jan Kaiser, Prof. Karen J. Heywood,
401 Dr Dorothee Bakker and Dr Jacqueline Boutin, funded by the Defence, Science and

402 Technology Laboratory (Contract no. DSTLX1000092277) with cooperation with Direction

403 Générale de l'Armement (DGA)-. The assistance of the UEA Glider Group in keeping the

404 glider flying is also gratefully acknowledged. The BOUSSOLE time series project is funded

405 by the Centre National d'Etudes Spatiales (CNES) and the European Space Agency

406 (ESA/ESRIN contract 4000119096/17/I-BG). The authors acknowledge Météo-France for

407 supplying the data from the Azur buoy and the HyMeX database teams (ESPRI/IPSL and

408 SEDOO/Observatoire Midi-Pyrénées) for their help in accessing their data. Crew and

409 Captains of R/V Tethys II are warmly thanked for assistance with operations at sea.

410

411 References

412 Álvarez, M., Sanleón-Bartolomé, H., Tanhua, T., Mintrop, L.,Luchetta, A., Cantoni, C.,

413 Schroeder, K., and Civitarese, G.: The CO2 system in the Mediterranean Sea: a basin wide

414 perspective, Ocean Sci., 10, 69–92, https://doi.org/10.5194/os-10-69-2014,2014.

415 Andersen, V. and Prieur, L.: One-month study in the open NW Mediterranean Sea

416 (DYNAPROC experiment, May 1995): Overview of hydrobiogeochemical structures and

417 effects of wind events, Deep-Sea Res. I, 47, 397–422, 2000.

418 Antoine, D. M. Chami, H. Claustre, F. D'Ortenzio, A. Morel, G. Bécu, B. Gentili, F. Louis ,J.

419 Ras, E. Roussier, A.J. Scott, D. Tailliez, S. B. Hooker, P. Guevel, J.-F. Desté, C. Dempsey

420 and D. Adams. 2006, BOUSSOLE : a joint CNRS-INSU, ESA, CNES and NASA Ocean

421 Color Calibration and Validation Activity. NASA Technical memorandum, N° TM-2006-

422 214147, NASA/GSFC, Greenbelt, USA.

423 Antoine, D., P. Guevel, J.-F. Desté, G. Bécu, F. Louis, A.J. Scott and P. Bardey: The

424 «BOUSSOLE» buoy; a new transparent-to-swell taut mooring dedicated to marine optics:

425 design, tests and performance at sea, Journal of Atmospheric and Oceanic Technology, 25,

426 968-989, 2008a.

427 Antoine, D., F. d'Ortenzio, S. B. Hooker, G. Bécu, B. Gentili, D. Tailliez, and A. J. Scott:

428 Assessment of uncertainty in the ocean reflectance determined by three satellite ocean color

429 sensors (MERIS, SeaWiFS and MODIS-A) at an offshore site in the Mediterranean Sea

430 (BOUSSOLE project), Journal of Geophysical Research, 113(C7), 2008b.

431   Begovic , M., and C. Copin-Montegut, Processes controlling annual variations in the partial

432   pressure of fCO2 in surface waters of the central northwestern Mediterranean sea (Dyfamed

433   site), Deep-Sea Research II, 49, 2031-2047, 2002

434   Behrenfeld, M. J, Abandoning Sverdrup's critical depth hypothesis on phytoplankton blooms.

435   Ecology, 91(4), 977-989, 2010

436   Behrenfeld, M. and E. Boss, Resurrecting the ecological underpinnings of ocean plankton

437   blooms. Annual Review of Marine Science, 6, 167-194, DOI: 10.1146/annurev-marine-

438   052913-021325, 2014

439   Brainerd, K. E., and Gregg, M. C, Surface mixed and mixing layer depths. Deep Sea Research

440   I: Oceanographic Research Papers, 42:1521–1543, 1995

441   Brody, S., and Lozier,M. Changes in dominant mixing length scale as a driver of

442   phytoplankton bloom initiation in the North Atlantic, Geophysical Research Letters 41, 3197–

443   3206, 2014.

444   Brody, S. R., & Lozier, M. S. , Characterizing upper-ocean mixing and its effect on the spring

445   phytoplankton bloom with in situ data. ICES Journal of Marine Science, 72(6), 1961-1970,

446   2015.

447   Chiswell, S. M.: Annual cycles and spring blooms in phytoplankton: don't abandon Sverdrup

448   completely. Marine Ecology Progress Series, 443, 39-50, 2011.

449   Copin-Montégut, C., Begovic, M.: Distributions of carbonate properties and oxygen along the

450   water column (0– 2000 m) in the central part of the NW Mediterranean Sea (Dyfamed site).

451   Influence of winter vertical mixing on air– sea CO2 and O2 exchanges. Deep-Sea Res., Part 2,

452   Top. Stud. Oceanogr. 49, 2049– 2066, 2002.

453   Copin-Montégut, C., M. Bégovic, and L. Merlivat.: Variability of the partial pressure of CO2

454   on diel to annual time scales in the Northwestern Mediterranean Sea, Mar Chem, 85(3-4),

455   169-189, 2004.

456   Coppola, L., Legendre, L., Lefevre, D., Prieur, L., Taillandier, V., & Riquier, E. D. :

457   Seasonal and inter–annual variations of dissolved oxygen in the northwestern Mediterranean

458   Sea (DYFAMED site). Progress in Oceanography, 2018.

459   Dickson, A. G., and F. J. Millero .: A comparison of the equilibrium constants for the

460   dissociation of carbonic acid in seawater media, Deep Sea Research Part A. Oceanographic

461   Research Papers, 34(10), 1733-1743 1987.

462   Enriquez, R.M., Taylor, J.R: Numerical simulations of the competition between wind-driven

463   mixing and surface heating in triggering spring phytoplankton blooms. ICES J. Mar. Sci. J. du

464   Cons. fsv071, 2015.

465   Golbol, M., Vellucci, V., Antoine, D .: BOUSSOLE, https://doi.org/10.18142/1, 2000.

466   Hemming, M. P., Kaiser, J., Heywood, K. J., Bakker, D. C., Boutin, J., Shitashima, K., Onken,

467   R. : Measuring pH variability using an experimental sensor on an underwater glider. Ocean

468   Science, 13 , 427–442,2017.

469   Holte, J., & Talley, L. : A new algorithm for finding mixed layer depths with applications to

470   Argo data and Subantarctic Mode Water formation. Journal of Atmospheric and Oceanic

471   Technology, 26(9), 1920-1939, 2009.

472   Hood, E. M., and L. Merlivat .: Annual and interannual variations of fCO2 in the

473   northwestern Mediterranean Sea: Results from hourly measurements made by CARIOCA

474   buoys, 1995-1997, J Mar Res, 59, 113-131, 2001.

475   Lacour, L., Briggs, N., Claustre, H., Ardyna, M., & Dall'Olmo, G.: The intraseasonal

476   dynamics of the mixed layer pump in the subpolar North Atlantic Ocean: A

477   Biogeochemical‐Argo float approach. Global Biogeochemical Cycles, 33(3), 266–281,2019.

478   Lee, Z., Weidemann, A., Kindle, J., Arnone, R., Carder, K. L., & Davis, C. : Euphotic

479   zone depth: Its derivation and implication to ocean-color remote sensing. Journal of

480   Geophysical Research: Oceans , 112 (C3),2007.

481   Mahadevan, A., D'asaro, E., Lee, C., & Perry, M. J. : Eddy-driven stratification initiates

482   North Atlantic spring phytoplankton blooms. Science, 337(6090), 54-58, 2012.

483   Marty, J.-C., Chiavérini, J. .: Seasonal and interannual variations in phytoplankton

484   production at DYFAMED time-series station, northwestern Mediterranean Sea. Deep

485   Sea Res. Part II 49, 2017–2030, 2002.

486 Mehrbach, C., C. H. Culberson, J. E. Hawley, and R. M. Pytkowicx .: Measurement of the
487 apparent dissociation constants of carbonic acid in seawater at atmospheric pressure, Limnol
488 Oceanogr, 18(6), 897-907, 1973.

489 Merlivat, L., and Brault, P.: CARIOCA BUOY, Carbon Dioxide Monitor, Sea Technol., 23–
490 30, 1995.

491 Merlivat, L., Boutin, J., & Antoine, D. : Roles of biological and physical processes in driving
492 seasonal air–sea CO 2 flux in the Southern Ocean: New insights from CARIOCA pCO 2.
493 Journal of Marine Systems, 147, 9-20, 2015.

494 Merlivat, L., Boutin, J., Antoine, D., Beaumont, L., Golbol, M., & Vellucci, V. : Increase of
495 dissolved inorganic carbon and decrease of pH in near surface waters of the Mediterranean
496 Sea during the past two decades. Biogeosciences, 15(18), 5653-5662, 2018.

497 Millot: Circulation in the Western Mediterranean Sea, Journal of Marine Systems, 20, 423–
498 442, 1999.

499 Morel, A., and J. F. Berthon . : Surface pigments, algal biomass profiles, and potential
500 production of the euphotic layer: relationships reinvestigated in review of remote-sensing
501 applications, Limnol. Oceanogr., 34, 1545–1562, 1989.

502 Niewiadomska, Katarzyna, Claustre, Hervé, Prieur, Louis, d'Ortenzio, Fabrizio, (2008),
503 Submesoscale physical‐biogeochemical coupling across the Ligurian current (northwestern
504 Mediterranean) using a bio‐optical glider, Limnology and Oceanography, 53, doi:
505 10.4319/lo.2008.53.5_part_2.2210.

506 Papaioannou, G., Papanikolaou, N., and Retalis, D. : Relationships of photosynthetically
507 active radiation and shortwave irradiance. Theoretical and Applied Climatology, 48: 23–27,
508 1993.

509 Pasqueron de Fommervault, O., Migon, C., D'Ortenzio, F., Ribera d'Alcalà, M., and Coppola,
510 L.: Temporal variability of nutrient concentrations in the northwestern Mediterranean sea
511 (DYFAMED time-series station), Deep-Sea Res. Pt. I, 100, 1–12, 2015.

512 Pellichero, V., Boutin, J., Claustre, H., Merlivat, L., Sallée, J.-B., & Blain, S. : Relaxation of
513 wind stress drives the abrupt onset of biological carbon uptake in the Kerguelen bloom: a

multisensory approach. Geophysical Research Letters,47,https://doi.org/10.1029/2019GL085992 , 2020.

Rödenbeck, C., Keeling, R. F., Bakker, D. C. E., Metzl, N., Olsen, A., Sabine, C., and Heimann, M.: Global surface-ocean pCO2 and sea–air CO2 flux variability from an observation- driven ocean mixed-layer scheme, Ocean Sci., 9, 193–216, doi:10.5194/os-9-193-2013, 2013.

Rumyantseva, A, Henson, S, Martin,A , Thompson, A. F, Damerell G.M, Kaiser J, Heywood, K.J.: Phytoplankton spring bloom initiation: The impact of atmospheric forcing and light in the temperate North Atlantic Ocean, Progress in Oceanography, 2019.

Siegel, D. A., S. C. Doney, and J. A. Yoder (2002), The North Atlantic spring phytoplankton bloom and Sverdrup's critical depth hypothesis, Science, 296, 730– 733.

Sverdrup, H. U.: On vernal blooming of phytoplankton. Conseil Exp. Mer, 18, 287-295,1953.

Takahashi, T., Sutherland, S. C., Wanninkhof, R., Sweeney, C., Feely, R. A., Chipman, D. W., Hales, B., Friederich, G., Chavez, F., Sabine, C., Watson, A., Bakker, D. C. E., Schuster, U., Metzl, N., Yoshikawa-Inoue, H., Ishii, M., Midorikawa, T., Nojiri, Y., Kortzinger, A., Steinhoff, T., Hoppema, M., Olafsson, J., Arnarson, T. S., Tillbrook, B., Johannessen, T.and Olsen, A., Bellerby, R., Wong, C. S., Delille, B., Bates, N. R., and de Baar, H. J. W.: Climatological mean and decadal change in surface ocean pCO2 and net sea-air CO2 flux over the global oceans, Deep-Sea Res. II, 56, 554–577, 2009.

Taylor, J. R., & Ferrari, R.: Shutdown of turbulent convection as a new criterion for the onset of spring phytoplankton blooms. Limnology and Oceanography, 56(6), 2293-2307, 2011.

Venables, H. and Moore, C.M.: Phytoplankton and light limitation in the Southern Ocean: Learning from high nutrient, high chlorophyll areas. Journal of Geophysical Research: Oceans, 115(C2), 2010.

Wanninkhof, R.: Relationship between wind speed and gas exchange over the ocean revisited. Limnology and Oceanography: Methods, 12(6), 351–362, 2014.

Weiss, R.: Carbon dioxide in water and seawater: the solubility of a non-ideal gas, Marine chemistry , 2 (3), 203–215, 1974

543

544   Figures and tables

545   Figure 1. The area of the northwestern Mediterranean Sea showing the French and Italian
546   Rivieras, the island of Corsica, the main current branches (green arrows) in the Ligurian Sea
547   and the location of the BOUSSOLE buoy (white square) and the AZUR meteorological buoy
548   (yellow square). The black line indicates the glider's path in March-April 2016.

549   Figure 2. 2016 (a) Hourly DIC (green) and SST(purple) at the BOUSSOLE site, (b) hourly
550   wind stress (blue) and net heat flux (pink) at the Azur buoy site. The pink dotted line indicates
551   the change of sign of the net heat flux from negative to positive values, (c) daily depths of the
552   mixed layer (black), mixing layer (dotted black), Ekman layer (cyan) and euphotic layer
553   (orange) at the BOUSSOLE site. The black dotted line on panels (a), (b), (c) (d) and (e)
554   indicates the onset time of the bloom (18 March). (d) PAR (orange) and average mixing layer
555   irradiance (blue), (e) Glider-derived depths of the mixed layer (black curve, same as in (c)),
556   euphotic layer (orange), and nighttime 2-day binned chlorophyll concentration (green
557   coloring) retrieved between March 7 and April 5.

558   Figure 3. (a, b, c) 2017, 2018 and 2019 DIC (green) and SST (purple) at the BOUSSOLE site,
559   (d, e, f) wind stress (blue) and net heat flux (red) at the Azur buoy site. The red dotted line
560   indicates the change of sign of the net heat flux from negative to positive values, (g, h, i)
561   depths of the mixing layer (dotted black), Ekman layer (cyan) and euphotic layer (orange) at
562   the BOUSSOLE site. The vertical dotted green line indicates the onset of the bloom.

563   Figure 4. Changes of physical parameters (hourly values) at the onset of the 2016 bloom
564   during 2 consecutive periods of 4 days, March 14-17 (blue) and March 18-21 (red) as a
565   function of wind stress (a) net surface heat flux (b) depths of the mixing layer. Grey circles
566   and grey squares indicate mean values respectively on March 17 and March 18. For
567   comparison, the orange line shows the euphotic layer depth (March 14-21).

568   Figure 5. From March 6 to April 5, (a) DIC and Chla. The purple line and the squares (blue
569   and grey) indicate the 3 days biological diurnal DIC changes during the period considered to
570   compute NCP. The blue and orange lines indicate the surface Chla when the glider was at a
571   distance of less than 5 km (blue) and less than 20 km (orange) respectively from the Boussole
572   buoy. (b) PAR and I average mixing layer. The vertical dotted black line indicates the onset of
573   the bloom on March 18.

574   Table 1. Net community production computed in the mixing layer over 3 days (NCP) after the
575   bloom onset (T_0). (a, b) variation of DIC at the measurement depth and linked correlation
576   coefficient; (c, d) change of integrated DIC over Z_{mx} and linked correlation coefficient ;(e)
577   CO_2 flux from the atmosphere to the ocean; (f), absolute value of calculated NCP is
578   considered in order to provide positive values throughout the presentation and discussion in
579   the manuscript.

580   Table 2. 2016-2019. Atmospheric drivers of the onset of the bloom: average values and
581   standard deviation on the day of the start of the bloom, T_0.

582